that P_{eqnx} may be written entirely in terms of a:

$$P_{eqnx} = 37{,}800\left[\left\{5.87 - 4.87\left(\frac{a}{a_0}\right)^{0.5}\right\}\left\{\left(\frac{a_0}{a}\right)^3 + 0.465\right\}\right]^{-1} \quad (7)$$

Since P_{eqnx} varies not only as a function of lunar distance but also as a function of the daylength through its impact on the equatorial bulge, it is possible, in principle, to determine the daylength directly.

The period of obliquity oscillations may be written as

$$P_{obl} = \left[\frac{1}{P_{eqnx}} - \frac{1}{P_{incl}}\right]^{-1} \quad (8)$$

where $P_{incl} = 68.8$ kyr for the most important term[24].

The perihelion precession is composed of four larger terms and a myriad of smaller ones[22,23]. These may be written in the form

$$P_{peri} = \left[\frac{1}{P_{eqnx}} + \frac{1}{P_{ecc}}\right]^{-1} \quad (9)$$

where the most important eccentricity periods are 308, 176, 72.6 and 75.3 kyr (ref. 23). These correspond to P_{peri} of 23.7, 22.4, 19 and 19.2 kyr, respectively.

The amplitude of the obliquity oscillation also varies[24]. This may be written approximately as

$$\Delta\gamma = 2.0° \frac{P_{eqnx}}{P_{incl} - P_{eqnx}} \quad (10)$$

As there are in fact half a dozen other periods associated with non-negligible, albeit lesser, inclination variations, equation (10) should really be written as a sum, the terms of which are given by Ward[24]. What is shown by equation (10) is that the magnitude of the obliquity oscillations is increasing, and that it was about 40% of its present value when the Weeli Wolli Formation was laid down.

We conclude that the Milankovitch periodicities that might be expected in the Weeli Wolli Formation or another formation of comparable age would be ~105, ~17 and ~13 kyr, respectively. The shorter of these might be associated with the alteration between BIF bands and S bands reported by Trendall[18] for the Dales Gorge Member of the Brockman iron formation.

This research was supported in part by NASA grant NAGW-176.

Received 6 November 1985; accepted 20 January 1986.

1. Lambeck, K. *The Earth's Variable Rotation* (Cambridge University Press, New York, 1980).
2. Trendall, A. F. *Econ. Geol.* **68**, 1089-1097 (1973).
3. Currie, R. G. *J. geophys. Res.* **86**, 11055-11064 (1981).
4. Currie, R. G. *J. geophys. Res.* **89**, 1295-1308 (1984).
5. Vines, R. G. *J. geophys. Res.* **87**, 7303-7311 (1982).
6. Currie, R. G. *J. geophys. Res.* **89**, 7215-7230 (1984).
7. Currie, R. G. *Geophys. Res. Lett.* **10**, 1089-1092 (1983).
8. Campbell, W. H., Blechman, J. B. & Bryson, R. A. *J. Clim. appl. Met.* **22**, 289-296 (1983).
9. Currie, R. G. *Geophys. Res. Lett.* **11**, 50-53 (1984).
10. Hameed, S., Yeh, W. M., Cess, R. D. & Wang, W. C. *Geophys. Res. Lett.* **10**, 436-439 (1983).
11. Hays, J. D., Imbrie, J. & Shackleton, N. J. *Science* **1294**, 1121-1132 (1976).
12. Crowley, T. J. *Rev. Geophys.* **21**, 828-877 (1983).
13. Lorius, C. *et al. Nature* **316**, 591-596 (1985).
14. Brosche, P. & Sündermann, J. (eds) *Tidal Friction and the Earth's Rotation* (Springer, New York, 1978).
15. Brosche, P. & Sündermann, J. (eds) *Tidal Friction and the Earth's Rotation* Vol. 2 (Springer, New York, 1982).
16. Cazenave, A. in *Tidal Friction and the Earth's Rotation* Vol. 2 (eds Brosche, P. & Sündermann, J.) 4-18 (Springer, New York, 1982).
17. Scrutton, C. T. in *Tidal Friction and the Earth's Rotation* (eds Brosche, P. & Sündermann, J.) 154-196 (Springer, New York, 1978).
18. Trendall, A. F. in *Iron Formations: Facts and Problems* (eds Trendall, A. F. & Morris, R. C.) 69-129 (Elsevier, New York, 1983).
19. Clegg, S. L. & Wigley, T. M. L. *Geophys. Res. Lett.* **11**, 1219-1222 (1984).
20. Hameed, S. *Geophys. Res. Lett.* 843-845 (1984).
21. Kaula, W. M. *An Introduction to Planetary Physics* (Wiley, Toronto, 1969).
22. Berger, A. *Astr. Astrophys.* **51**, 127-135 (1976).
23. Berger, A. *J. atmos. Sci.* **35**, 2362-2367 (1978).
24. Ward, W. R. *Icarus* **50**, 444-448 (1982).
25. Goldreich, P. *Rev. Geophys.* **4**, 411-439 (1966).

Sahel rainfall and worldwide sea temperatures, 1901–85

C. K. Folland, T. N. Palmer & D. E. Parker

Meteorological Office, London Road, Bracknell RG12 2SZ, UK

Using the comprehensively quality-controlled Meteorological Office Historical Sea Surface Temperature data set (MOHSST)[1,2] we show for the first time that persistently wet and dry periods in the Sahel region of Africa are strongly related to contrasting patterns of sea-surface temperature (SST) anomalies on a near-global scale. The anomalies include relative changes in SST between the hemispheres, on timescales of years to tens of years, which are most pronounced in the Atlantic. Experiments with an 11-level global atmospheric general circulation model (AGCM) support the idea that the worldwide SST anomalies modulate summer Sahel rainfall through changes in tropical atmospheric circulation[3–6]. El Niño events may also play a part. We do not discount the effects of soil moisture and albedo changes in the Sahel[7,8], although Courel *et al.*[9] have questioned the importance of albedo changes, but we do suggest that worldwide SST anomalies may have a more fundamental influence on Sahel rainfall.

Rainfall records for sub-Saharan North Africa have been collated and normalized by many authors. We have used an

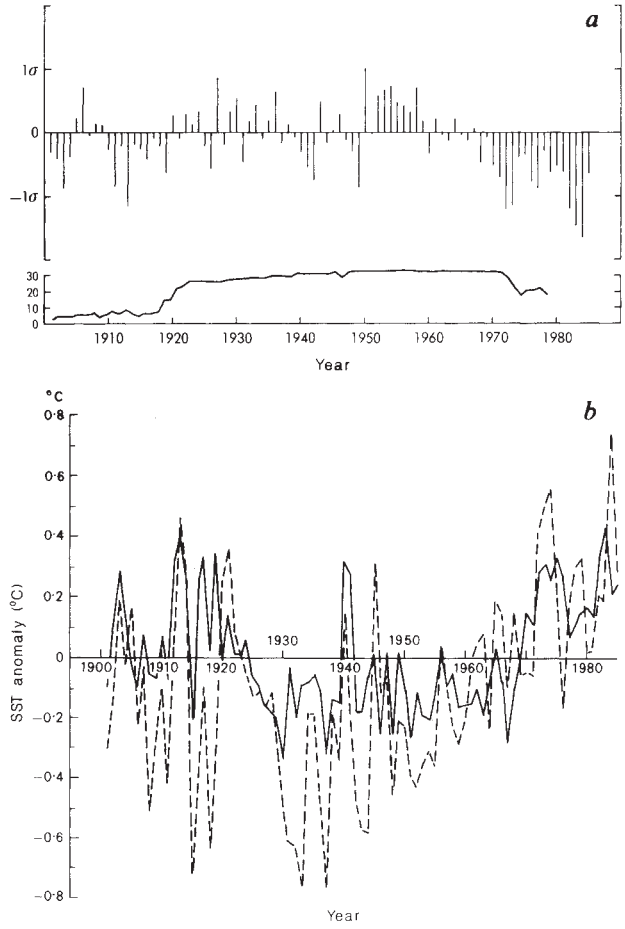

Fig. 1 *a*, Standardized annual rainfall anomalies for the Sahel, 1901-85 (upper panel). Values to 1984 are after Nicholson[11]; 1985 values are from CLIMAT reports. The lower panel gives the numbers of stations used. *b*, SST anomalies (relative to 1951-80), for July to September 1901-85. Solid line, Southern Hemisphere with the Northern Indian Ocean, minus the rest of the Northern Hemisphere (SHNI − RNH). Dashed line, South Atlantic minus North Atlantic.

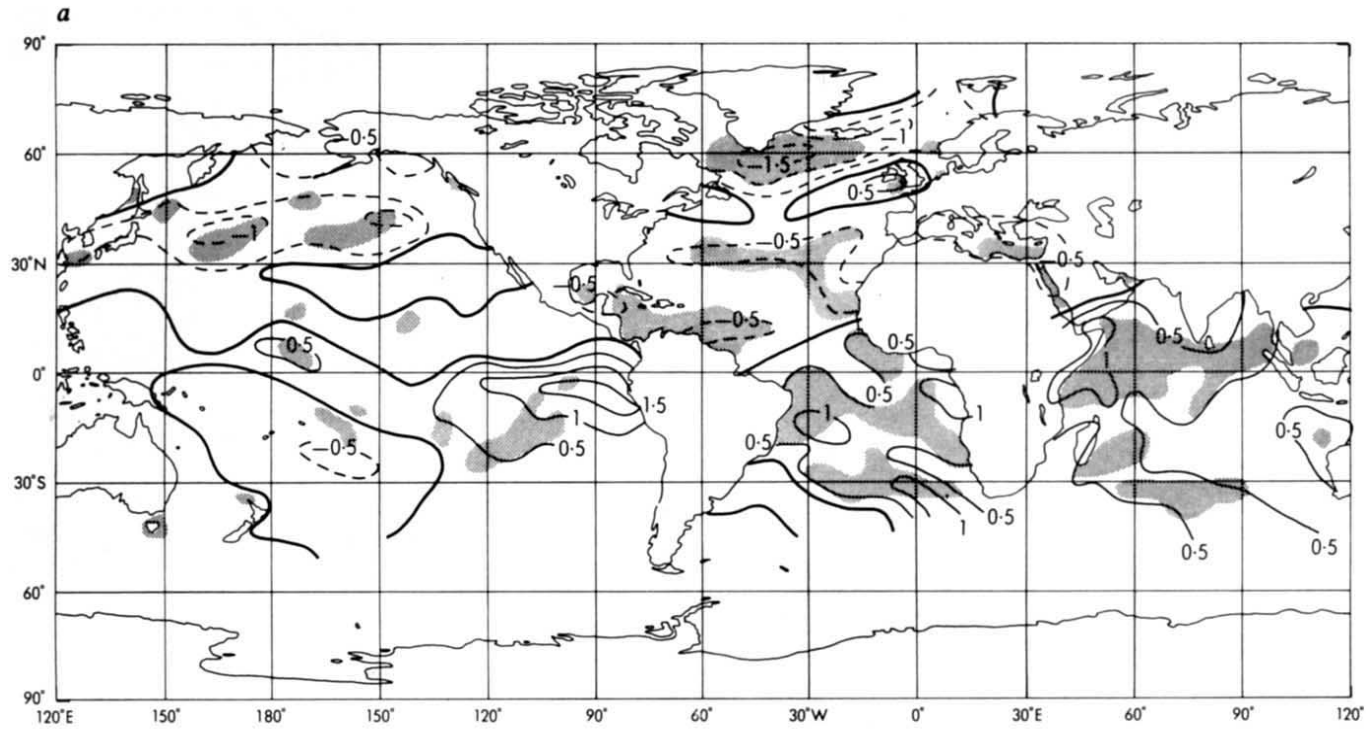

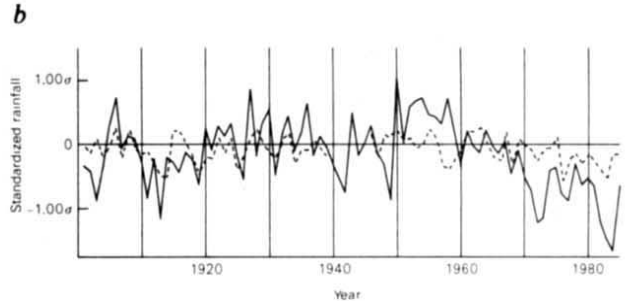

Fig. 2 *a*, SST, July to September: average of (1972–73, 1982–84) (Sahel dry) minus average of (1950, 1952–54, 1958) (Sahel wet). Contours every 0.5 °C. Shaded areas are different from zero at the 90% level of significance according to a *t*-test. *b*, Observed (——) and simulated (– –) Sahel rainfall (see text).

updated version of Nicholson's[10,11] annual Sahel series for 1901–84 (Fig. 1*a*) supplemented by CLIMAT reports for 1985 (see ref. 10 for a map of the area, which stretches from Senegal to Sudan at approximately 14–18° N). Nicholson homogenized her data to allow for the use of widely differing numbers of stations through time.

Most rain falls in June or July to September and is associated with the seasonal movement of the Intertropical Convergence Zone (ITCZ). Kidson[12], Lamb[3] and Newell and Kidson[4] suggested that a contributory reason for drier Sahel summers may be a weaker-than-average convergence of the mean moisture flux into West Africa. Newell and Kidson[4] found that the lower tropospheric south-westerly winds were shallower and weaker in the dry years, although near the surface they tended to penetrate almost as far north as in most wet years. Variations in the northward penetration of the ITCZ cannot be completely neglected but are not thought to be a major determinant of Sahel rainfall, as was once suggested by Winstanley[13], but afterwards challenged[14].

Based on a hemispheric general circulation model, it was suggested in 1974 that cooler than normal SSTs in the tropical North Atlantic in summer might reduce west Sahel rainfall (A. Gilchrist, unpublished data). Lamb[6], Lough[15] and Hastenrath[5] have demonstrated from observations that large-scale SST anomalies in the tropical North and South Atlantic have probably modulated Sahel rainfall in some recent years, although Lough could find no such links prior to 1940. For a different season, Moura and Shukla[16] have used a numerical model to substantiate the influence of tropical Atlantic SST anomalies on rainfall in the Brazilian Nordeste.

Using more complete SST data than previously available, Folland and coworkers[1,2] provide hints that the present drought epoch might be linked with global scale changes in SST. After 1960–65, marked warming of the Southern Hemisphere and simultaneous cooling of the Northern Hemisphere oceans is observed; the latter reversed before 1980, since when both hemispheres have warmed. However, the North Indian Ocean has tended to warm nearly in phase with the Southern Hemisphere, with strong cooling in the North Pacific and North Atlantic until recently. Figure 1b shows annual July–September SST anomalies for 1901–85 (from a 1951–80 average) for the Southern Hemisphere and North Indian Ocean together (SHNI), minus the remainder of the Northern Hemisphere (RNH) and for the South minus the North Atlantic Ocean. These regional and worldwide trends have been noted and their reality assessed by many authors[17–23], using less complete and less well quality-controlled data (except for some North Pacific studies). Problems of separating climatic signals from instrumental biases in marine data have recently been stressed[24,25]. Strongest support for Fig. 1*b* comes from the pattern of the second empirical orthogonal function of worldwide SST anomalies calculated for all seasons for 1964–79 by Hsiung and Newell[20].

The data in Fig. 1 indicate a marked tendency for a relatively warm (cold) SHNI to be associated with drier (wetter) epochs or (sometimes) individual years in the Sahel. The Atlantic curve gives a less clear association (Table 1); thus, any forcing of Sahel rainfall by large-scale SST anomalies may be on a worldwide rather than an Atlantic scale. Rind and Rossow[26] have recently drawn attention to the likely sensitivity of the Hadley circulations to very-large-scale changes in SST.

Figure 2*a* shows a worldwide SST difference field for July to September on a 5° × 5° spatial scale between the five driest and

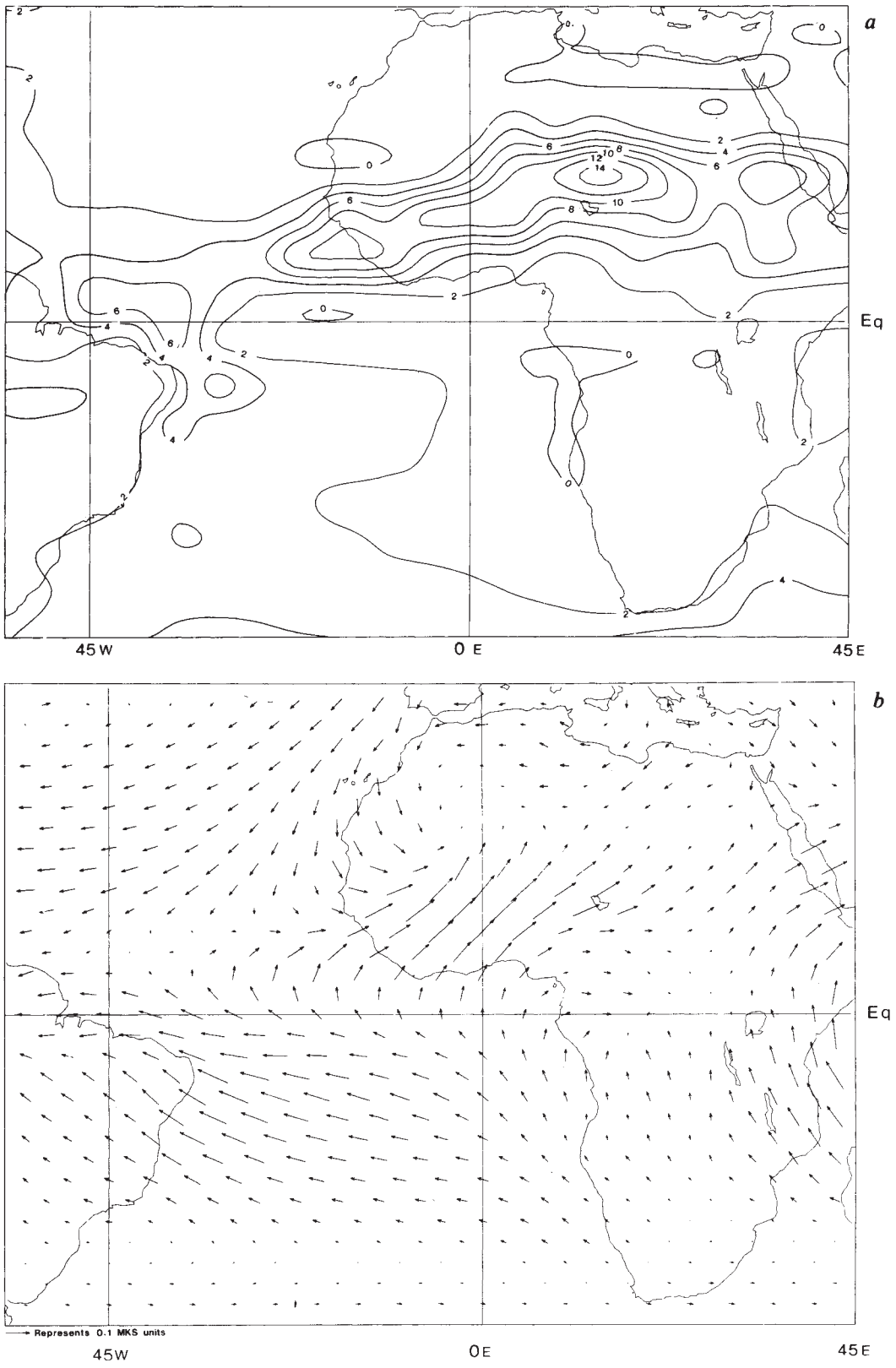

Fig. 3 *a*, Mean rainfall (millimetres per day) in a 180-day control run. *b*, Average 950-mbar steady moisture flux in a 180-day control run. *c*, 180-Day mean rainfall (millimetres per day); anomaly integration minus control. *d*, 180-Day mean 950-mbar steady moisture flux; anomaly integration minus control. The scale of the arrows shown in panel *d* is 5 times that in *b*.

five wettest rainfall seasons in the Sahel since 1945. Differences significant at the 90% level cover 24% of the analysed area, and the pattern is remarkably strong. Figure 2*a* shows that the whole Indian Ocean, South Atlantic and south-east Pacific are warm, while the North Atlantic, North Pacific and Mediterranean are cold. This SST difference pattern reflects a shift in areas of warmest tropical ocean; in particular, areas most subject to deep convection[27], that is warmer than 26 °C, are reduced and displaced slightly southward in the Atlantic but considerably increased in size in the western Indian Ocean. The warmth of the tropical south-east and central Pacific in very dry Sahel years reflects the influence of the 1972–73 and 1982–83 El Niño events. A worldwide SST difference pattern corresponding to the eight driest minus the eight wettest Sahel seasons before 1940 gives less clear warmth in the Indian and South Atlantic oceans (except the Gulf of Guinea) in the dry years, although the North

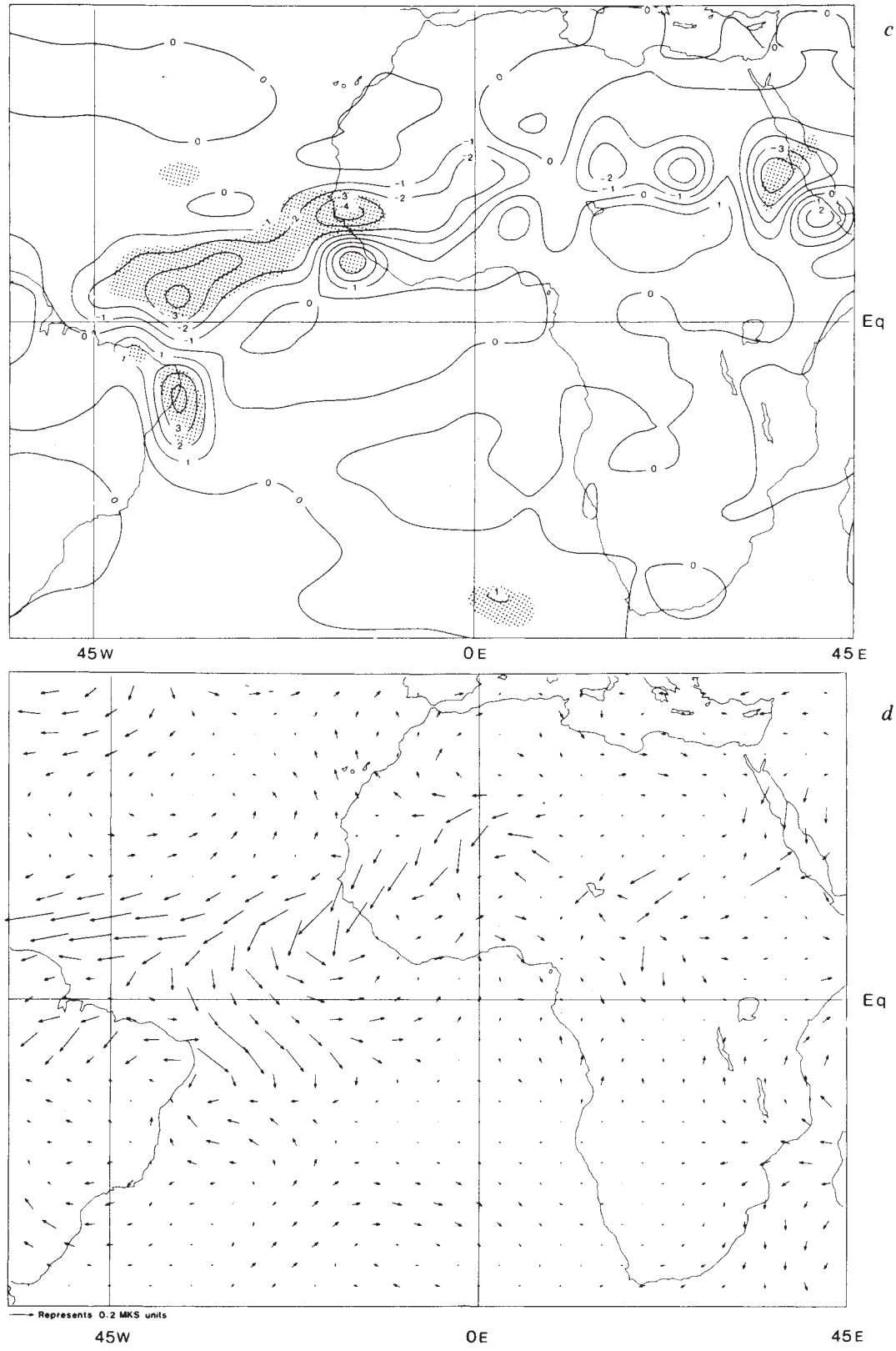

Pacific, North Atlantic and Mediterranean are still cool. An El Niño signature is also absent. Despite the poorer SST and rainfall data prior to 1945, the differences in the patterns may be partly genuine; the driest Sahel years before 1945 tended to accompany relatively wet conditions in West Africa around 9–11° N (Nicholson's[10] Soudano-Guinea series), whereas after 1945 most of western tropical Africa was dry when the Sahel was very dry. Thus the SST anomaly pattern associated with 'Sahel drought' is unlikely to be unique.

If Fig. 2*a* represents an important SST anomaly pattern that modulates Sahel rainfall on several timescales, it is reasonable to estimate indices of the similarity of each year (in the interval 1901–85) to this pattern (pattern (1)) and to the pattern observed prior to 1940 (pattern (2)) and to correlate both sets of indices year by year with Sahel rainfall. Each index was defined as a modified measure of the covariance between worldwide SST

Table 1 Correlation of July to September SST time series and Sahel rainfall, 1901–84

No.	Ocean SST series	r	S	σ_0 (°C)	c	m
1	Southern minus Northern hemisphere	−0.56	**	0.18	−0.15	−1.69
2	SHNI − RNH	−0.62	***	0.19	−0.15	−1.78
3	South − North Atlantic (0–30° S, 0–30° N)	−0.36		0.32	−0.19	−0.60
4	South − North Atlantic	−0.44	*	0.32	−0.24	−0.75
5	As 4 but with division at 5° N	−0.46	*	0.32	−0.25	−0.77
6	South Atlantic + S. Indian + N. Indian + East Tropical Pacific − N. Atlantic − N. Pacific − Mediterranean	−0.67	***	0.96	−0.23	−0.38
7	As 6 but ocean areas weighted according to size	−0.62	***	0.26	−0.09	−1.26
8	As 6 but with Atlantic split at 5° N	−0.69	***	0.96	−0.23	−0.39

r, Correlation coefficient; S, significance of r (assuming only 32 degrees of freedom because of lag-autocorrelation). *, =95%, **, =99%; ***, =99.9%; σ_0, Standard deviation of SST series (°C); c, regression constant (units are standardized Sahel rainfall); m, regression slope.

anomalies and the SST difference pattern:

$$I_{jm} = \sum_{i=1}^{n} (\mathrm{SSTA}_{ij} \times \Delta T_{im}) - G_j$$

$SSTA_{ij}$ is the SST anomaly in the 5° × 5° area i, in year j; and ΔT_{im} is the SST difference in Fig. 2*a* ($m = 1$) or that prior to 1940 ($m = 2$). G_j is a correction for fluctuations (from the 1951–80 average) in the mean SST measured over the whole pattern, which effectively removes global mean SST trends and instrumental biases. I_{jm} therefore reflects relative SST changes on a large scale. The correlations of I_{jm} with Sahel rainfall for 1901–84 were −0.72 (99.9% significant) for pattern (1) and −0.56 (99% significant) for pattern (2). For 1901–39 they were −0.43 (95% significant; pattern (1)) and −0.76 (99.9% significant; pattern (2)) and for 1946–84 the correlations were −0.85 and −0.48. (The significance of these data is hard to assess because of high autocorrelation between successive years' rainfall).

A stern test of any similarity in the influence of SST patterns (1) and (2) is to calculate the best linear regression equation between I_{jm} and Sahel rainfall S_j for the epoch of the SST difference pattern concerned, and to use the equation to simulate (that is, to predict using simultaneously observed SST anomalies) Sahel rainfall in the independent epoch. Simulated rainfalls for 1901–39 and for 1946–85, derived from I_{j1} and I_{j2} respectively, are plotted with the original values in Fig. 2*b*. The correlations between observed and simulated rainfall are 0.43 (30 degrees of freedom) and 0.48 (4 d.f.) respectively. These results suggest that a common forcing pattern is present in the summer SST anomaly patterns in both epochs despite a great change in the statistical structure of the Sahel rainfall series, which was dominated by large yearly variability before 1940 but was highly persistent after 1950.

We have carried out numerical experiments with the UK Meteorological Office 11-level AGCM (described by A. Slingo in the unpublished report Met 0 20 DCTN 29, September 1985) to gain more insight into the influence of the SST anomaly difference pattern shown in Fig. 2*a*. We ran the model in perpetual July mode for 180 days, first with fixed climatological average July SSTs and then with the SST anomaly pattern of Fig. 2*a* superimposed on the climatological values. Figure 3*a* shows the model's Sahel rainfall with climatological SSTs; the response of an AGCM to a particular SST anomaly is strongly dependent on its climatology without the anomaly[28]. Over the western and central Sahel, between about 15° W and 10° E, the model's rainfall climatology is in good agreement with Jaeger's[29] observed climatology. East of this region, the model's climatological rainfall extends north and south of the observed limits; the maximum northeast of Lake Chad is excessive. Over the western Sahel, model rainfall exceeds evaporation (not shown) by about 4 mm per day and moisture is supplied to this region by the horizontal moisture flux. The 'steady' component of this flux (that is, mean moisture field × vector mean wind) is shown in Fig. 3*b* for the 950 mbar level.

Figure 3*c* shows the rainfall in the integration with the observed composite SST anomaly, minus the control rainfall. Over the western Sahel, rainfall is decreased on average by about 30% of the model's climatological values. Over the eastern Sahel, there is a smaller but coherent reduction of about 1–2 mm per day, with reductions of up to 50% over the mountains of south-east Sudan and north-east Ethiopia. Figure 3*d* shows that the model's steady 950 mbar flux of moisture from the South Atlantic into the western Sahel is decreased by about 20–50%. This experiment therefore shows that the observed SST difference pattern of Fig. 2*a* can provide a coherent change in Sahel rainfall, mainly through a reduction in moisture flux convergence, with perhaps a small southward displacement of the ITCZ in the western Sahel. The effect of warmer SSTs in the Southern Hemisphere in increasing low-level saturation mixing ratios may therefore be much less important than the impact of the SST anomalies on the dynamics of the tropical atmosphere. This conclusion is consistent with the reduced divergence at 250 mbar in the model (not shown) over almost the whole Sahel belt, from south of 10° N up to 20° N and from the Atlantic to the Red Sea.

In a companion paper[30], the responses of the AGCM to individual composite SST anomalies in the Atlantic, Pacific and Indian oceans are tested individually. Although the Atlantic had the strongest effect on rainfall over the western Sahel, the Pacific anomalies also had a strong effect, and none of the individual ocean anomalies gave as large an effect as the worldwide pattern of Fig. 2*a*. It is likely that the Pacific influences Sahel rainfall through the generation of anomalous upper tropospheric westerlies across tropical Africa, similar to those from a northern winter El Niño SST anomaly[28]. The influence of the Indian Ocean in reducing modelled Sahel rainfall appears to be largest over Sudan and Northern Ethiopia. A full understanding of the effects of SST on Sahel rainfall requires consideration of the global oceans.

Received 26 October 1985; accepted 24 February 1986.

1. Folland, C. K., Parker, D. E. & Kates, F. E. *Nature* **310,** 670–673 (1984).
2. Folland, C. K., Parker, D. E. & Newman, M. R. *Proc. 9th Clim. Diags Conf.*, Corvallis, Oregon, 22–26 Oct. 1984, 70–85 (National Oceanic and Atmospheric Administration).
3. Lamb, P. J. *Tellus* **35A,** 198–212 (1983).
4. Newell, R. E. & Kidson, J. W. *J. Clim.* **4,** 27–33 (1984).
5. Hastenrath, S. *Mon. Weath. Rev.* U.S. Dep. Agric. **112,** 1097–1107 (1984).
6. Lamb, P. J. *Tellus* **30,** 240–251 (1978).
7. Cunnington, W. M. & Rowntree, P. R. *Q.J. R. met. Soc.* **112,** (in the press).
8. Charney, J. G., Quirk, W. J., Chow, S. H. & Kornfield, J. *J. atmos. Sci.* **34,** 1366–1385 (1977).
9. Courel, M. F., Kandel, R. S. & Rasool, S. I. *Nature* **307,** 528–531 (1984).
10. Nicholson, S. E. *Mon. Weath. Rev.* U.S. Dep. Agric. **108,** 473–487 (1980).
11. Nicholson, S. E. *J. Clim. appl. Met.* **24,** 1388–1391 (1985).
12. Kidson, J. W. *Q. Jl Roy. met. Soc.* **103,** 441–446 (1977).
13. Winstanley, D. *Nature* **243,** 464–465 (1973).
14. Miles, M. K. & Folland, C. K. *Nature* **252,** 616 (1974).
15. Lough, J. M. *Clim. Monit.* **9,** 150–157 (1980); *Mon. Weath. Rev. U.S. Dep. Agric.* **114** (in the press).
16. Moura, A. D. & Shukla, J. *J. atmos. Sci.* **38,** 2653–2675 (1981).
17. Bunker, A. F. *Mon. Weath. Rev. U.S. Dep. Agric.* **108,** 720–732 (1980).
18. Kukla, G. J. *et al. Nature* **270,** 573–580 (1977).
19. Newell, R. E. & Hsiung, J. *Riv. Ital. Geofis. Sci. Affini* **5,** 121–125 (1979).

20. Hsiung, J. & Newell, R. E. *J. phys. Oceanogr.* **13**, 1957-1967 (1983).
21. Paltridge, G. & Woodruff, S. *Mon. Weath. Rev. U.S Dep. Agric.* **112**, 1093-1095 (1984).
22. Douglas, A., Cayan, D. & Namias, J. *Mon. Weath. Rev.* U.S. Dep. Agric. **110**, 1851-1862 (1982).
23. Cadet, D. L. & Diehl, B. C. *Mon. Weath. Rev.* U.S. Dep. Agric. **112**, 1921-1935 (1984).
24. Barnett, T. P. *Mon. Weath. Rev. U.S. Dep. Agric.* **112**, 303-312 (1984).
25. Oort, A. H. & Maher, M. C. in *Coupled Ocean-Atmosphere Models* (ed. Nihoul, J.) 183-198 (Elsevier, Amsterdam, 1985).
26. Rind, D. & Rossow, W. B. *J. atmos. Sci.* **41**, 479-507 (1984).
27. Gadgil, S., Joseph, P. V. & Joshi, N. V. *Nature* **312**, 141-143 (1984).
28. Palmer, T. N. and Mansfield, D. A. *Q. J. R. met. Soc.* (in the press).
29. Jaeger, L. *Berichte Deutscherwetterd* Vol. 18, No. 139 (1976).
30. Palmer, T. N. *Nature* (in the press).

Glaciers as indicators of a carbon dioxide warming

J. Oerlemans

Institute of Meteorology and Oceanography, University of Utrecht, Princetonplein 5, Utrecht, The Netherlands

During the past 150 years, mountain glaciers have shown a worldwide retreat. It has been argued that this is related to the warming which is predicted to result from increased carbon dioxide levels in the atmosphere; however, this warming has not been detected in a statistically significant way from instrumental records. I demonstrate here that the lower part of a valley glacier is extremely sensitive to a local warming, induced by an increase in the radiation budget. For glaciers covering only a small fraction of a valley, the effect is particularly dramatic. Thus valley glaciers may be extremely vulnerable to the presence of infrared-absorbing gases in the atmosphere, and could therefore be better detectors of a possible carbon dioxide warming than is generally assumed.

Climatic indicators such as tree-ring width, sea level and glacier variations can extend our knowledge of the Earth's climatic history beyond the relatively recent period covered by instrumental records. In Europe, the presence of long valley glaciers in areas that have been populated for hundreds of years provides long records of glacier front variations. Figure 1 shows records of three glaciers in the Alps and one in Norway (Nigardsbreen)[1-5]. The dramatic retreat of these large glaciers since 1850 is generally believed to be part of a worldwide retreat, which contributed significantly to the observed rise in global sea level[6]. It is therefore natural to ask whether our knowledge of historic glacier variations can be of some value with regard to the carbon dioxide issue.

Many factors affect the annual mass balance of a glacier[7-10]; depending on type of glacier and climatic conditions, these include winter accumulation, summer temperature, cloudiness and early summer snowfall. Here I concentrate on melting rates at the lower parts of long glaciers, such as those referred to in Fig. 1. Such glaciers have their snout at altitudes where mean air temperature is far above the melting point in summer, and advective transfer of heat from regions surrounding the glacier is a very important factor. As will be demonstrated, this advective transfer amplifies the sensitivity of melting rates to changes in the radiation budget.

The calculation described below is based on a highly simplified model of the energy budget of a valley-glacier system, in which a daily cycle is obtained for four dependent variables; namely, surface temperature of the glacier (θ_s), surface temperature of the surrounding regions (T_s), mean boundary-layer temperature over the glacier (θ_a) and mean boundary-layer temperature over the surrounding regions (T_a). Here, the surface temperature is the mean temperature of the surface layer involved in the daily cycle, and the boundary-layer temperature is the mean air temperature in the lowest 1-1.5 km of the atmosphere.

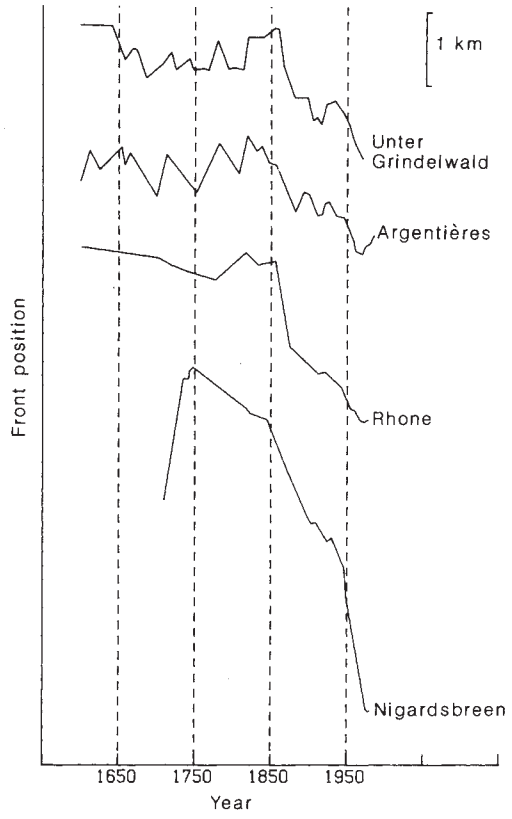

Fig. 1 Front variations of three valley glaciers in the Alps and one in Norway (Nigardsbreen). Data from refs 1-5. The retreat since 1850 is striking.

A diagram of the model is shown in Fig. 2. There are four boxes which interact by radiative processes (single arrows) and by turbulent and advective heat fluxes (double arrows). The surface layers also lose energy to space: a small part of the outgoing infrared flux escapes directly. The background atmosphere has a prescribed characteristic temperature T_b, so the radiation balance of this layer is irrelevant. Absorption of solar radiation in the boundary layer is ignored, so the model is forced by the absorption of solar energy at the surface.

The boundary is assumed to have an effective long-wavelength emissivity μ, while that of the background atmosphere is denoted by ν. The radiation balance of the surface layer (surrounding ground) can then be formulated as:

$$R_s = AQ(t) - \sigma T_s^4 + \mu\sigma T_a^4 + (1-\mu)\nu\sigma T_b^4, \qquad (1)$$

and the expression for the boundary layer is:

$$R_a = \mu\sigma T_s^4 - 2\mu\sigma T_a^4 + \mu\nu\sigma T_b^4 \qquad (2)$$

In equation (1), the first term on the right-hand side represents the absorption of solar radiation at the surface (Q is incident radiation, A effective absorptivity), the second term the upward long-wavelength emission, and the third and fourth terms counter-radiation from the atmosphere. σ is the Stefan-Boltzmann constant. The interpretation of equation (2) is similar, but there is no short-wavelength (solar) contribution. Equivalent equations can be written for the glacier, but the absorptivity will generally be lower.

A few comments on the effective absorptivity A are in order. In the present schematic calculation, effects such as those of cloud cover and atmospheric dust content are all absorbed in this quantity. A simply indicates what fraction of the solar radiation incident at the top of the atmosphere is absorbed at the surface. This implies that in the sensitivity experiments